

Article

Numerical Simulation of Material Flow and Analysis of Welding Characteristics in Friction Stir Welding Process

Haitao Luo ^{1,2,*} , Tingke Wu ^{1,3}, Peng Wang ^{1,4}, Fengqun Zhao ^{1,3}, Haonan Wang ^{1,4} and Yuxin Li ^{1,4}

¹ State Key Laboratory of Robotics, Shenyang Institute of Automation, Chinese Academy of Sciences, Shenyang 110016, China; wutingke@sia.cn (T.W.); 1710107@stu.neu.edu.cn (P.W.); zhaofengqun@sia.cn (F.Z.); 1770174@stu.neu.edu.cn (H.W.); liyuxin@stumail.neu.edu.cn (Y.L.)

² Institutes for Robotics and Intelligent Manufacturing, Chinese Academy of Sciences, Shenyang 110016, China

³ School of Mechanical Engineering, Shenyang Ligong University, Shenyang 110159, China

⁴ Institute of Mechanical Engineering and Automation, Northeastern University, Shenyang 110819, China

* Correspondence: luohaitao@sia.cn; Tel.: +86-131-3021-6191

Received: 5 May 2019; Accepted: 25 May 2019; Published: 28 May 2019



Abstract: Friction stir welding (FSW) material flow has an important influence on weld formation. The finite element model of the FSW process was established. The axial force and the spindle torque of the welding process were collected through experiments. The feasibility of the finite element model was verified by a data comparison. The temperature field of the welding process was analyzed hierarchically. It was found that the temperature on the advancing side is about 20 °C higher than that on the retreating side near the welding seam, but that the temperature difference between the two sides of the middle and lower layers was decreased. The particle tracking technique was used to study the material flow law in different areas of the weld seam. The results showed that part of the material inside the tool pin was squeezed to the bottom of the workpiece. The material on the upper surface tends to move downward under the influence of the shoulder extrusion, while the material on the lower part moves spirally upward under the influence of the tool pin. The material flow amount of the advancing side is higher than that of the retreating side. The law of material flow reveals the possible causes of the welding defects. It was found that the abnormal flow of materials at a low rotation speed and high welding speed is prone to holes and crack defects. The forming reasons and material flow differences in different regions are studied through the microstructure of the joint cross section. The feasibility of a finite element modeling and simulation analysis is further verified.

Keywords: material flow; finite element model; temperature field; microstructure; welding defects

1. Introduction

Friction stir welding (FSW) has achieved great success in joining aluminum alloys since its invention. Due to the characteristics of a high joint quality, small welding deformation, green welding process and no pollution, FSW technology is often applied to the welding of aluminum, magnesium and other light alloy materials [1–3]. High-strength aluminum alloys are used in the welding of aerospace products. Because of its good strength and hardness, 2XXX aluminum alloy is used for the welding of rocket storage tanks and aircraft wings [4,5]. However, FSW is a complicated thermal-mechanical coupling process, and the forming quality is mainly affected by the tool shape, rotation speed, welding speed and other process parameters [6–8]. If it is not properly controlled, it is easy to change the physical quantities, such as the heat generation and plastic flow state of the weld materials, which will lead to welding defects [9]. The material flow has an important influence on the quality of the

weld forming. Studying the material flow will help to understand the welding process and prevent welding defects.

In FSW, there is a close contact between the tool and the material to be welded, so there is severe friction between the tool and the workpiece. During the welding process, the intense friction between the tool and the workpiece generates a large amount of heat. This heat causes the temperature of the material to rise, and the material softens at high temperatures [10–12]. The softened material undergoes severe plastic flow under the drive of the tool. At the same time, the shear deformation of the material also generates a part of the heat [13]. Along with the plastic flow of the material at a high temperature, the heat transfer inside the material is convective and conductive. The severe plastic flow of the material under the drive of external force causes heat convection, and the temperature distribution also affects the plastic flow of the material [14,15].

Franke et al. [16] examines the intermittent flow of material and its relation to defect formation. In addition, advances have been made in a force-based defect detection model that links changes in process forces to the formation and size of defects. Gratecap et al. [17] placed a steel powder mark on the butt to study the material flow. The results show that the material in the weld zone extrudes around the retreating side (RS) of the tool pin as it moves from the leading side to the trailing side. Huang et al. [18] observed the vertical flow behavior of the material by observing the distribution of Cu foil fragments and Al-Cu intermetallic compounds. The downward and upward flows encounter each other at the advancing side (AS) in the material depositing process, changing the morphology of the weld nugget zone. Dialami et al. [19] used the fourth-order Runge-Kutta (Rk4) integration method to calculate the particle trajectory. The effect of the input process parameters and pin shape on the weld quality was studied by a particle tracking method.

Li et al. [20] added a 0.1 mm thick bronze foil to the 7075-T651 aluminum alloy welding interface. The distribution characteristics of the horizontal and vertical cross-section bronze foil were analyzed by X-ray. They measured that the shear force at the front of the tool was stronger than the shear at the back of the tool pin. The metal is mainly sheared from the advancing side in front of the tool to the retreating side. Then, under the squeezing force of the rotary tool, the plastic material is pushed back to the advancing side at a slow speed. As a result, a temporary cavity is formed on the advancing side. The plasticized material is extruded into a cavity and filled therein. Figure 1 shows a schematic of the flow of material around the tool. Shanavas and Dhas [21] discussed the development of fuzzy models for predicting the weld quality. The effects of welding parameters, such as the tool geometry, tool rotation speed, welding speed and tool inclination angle, on the welding quality are studied. De Filippis et al. [22] established a simulation model to monitor, control and optimize the friction stir welding process. The correlation between the process parameters and mechanical properties can be identified. In order to improve the welding performance, the parameters of the joint are controlled in real time through experiments. Cisco et al. [23] conducted a large number of experiments and calculations on the fatigue behavior of aluminum-lithium alloy (AA2099) friction stir welding (FSW). The effect of the friction stir welding process on the fatigue life was studied by using a microstructure sensitive fatigue model.

Zhang et al. [24] proposed a conceptual model describing weld formation to study the effect of the Alclad layer on material flow and defect formation. He found that the top Alclad assembled at the shoulder/workpiece interface, thereby weakening the material flow in the shoulder-driven zone and favoring the formation of a void defect at high traveling speeds. Zhu et al. [25] established a three-dimensional coupled finite element model of friction stir welding defects based on the Euler-Lagrange coupling method. The results show that smaller gaps will be generated at higher welding speeds.

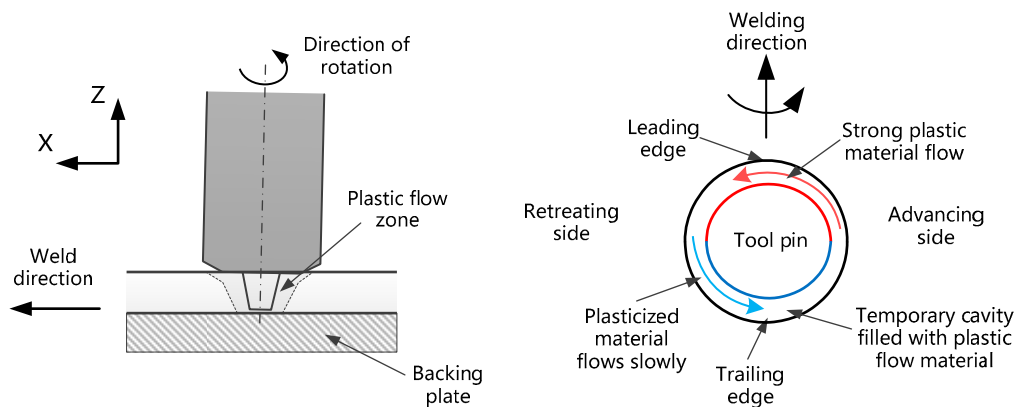


Figure 1. Schematic of the material movement around the friction stir welding (FSW) tool.

Although some scholars have conducted some research on material flow [26–28], the numerical model is still in the initial stage, and there are still many problems to be studied. According to the author’s knowledge, there is no report about the process from the plunging process to the material staying behind the weld. This paper understands the frictional heat generation of the tool and the material by establishing the heat input model. A finite element model was constructed to simulate the AA2A14-T6 friction stir welding process. The axial force and torque of the welding process were collected by electromagnetic coupling technology and compared with the simulation data. The results verified the correctness of the finite element model.

The contribution of this article is to establish the thermogenic physical model of the FSW process and to establish the finite element model of FSW. The material flow and temperature fields of the welding process are studied by a numerical simulation. The numerical simulation results are further verified by using the microstructure of the weld. Through the stratified analysis of the temperature of the weld zone, it was found that the advancing side and the retreating side above the material showed obvious temperature differences, and this phenomenon was also found in the test [29]. A material flow analysis was carried out on the inside of the stirring pin via particle tracking technology. It was found that a small part of the internal material of the pin was extruded to the bottom of the weld and that most of the materials moved upward with the pin. A material flow analysis was performed on the advancing side and the retreating side of the welded area, respectively. The material flow exhibits different flow conditions on the advancing and retreating sides. At the same time, a similar situation was found through the microstructure of the joint. The analysis of the flow trend of the microstructure confirmed the correctness of the finite element analysis. Since the material flow is closely related to the weld formation, this paper can predict or provide a reference for future welding experiments by analyzing the defects of the finite element model.

2. Modeling and Acquisition Methods

2.1. Friction Stir Welding Heat Input Model

The heat input of friction stir welding makes the plastic flow of materials a complex process, which is accompanied by the coupling and interaction of the friction heat generation, metal plastic flow and structural transformation. Therefore, it is very difficult or even impossible to carry out a comprehensive analysis of all factors in the friction stir processing (FSP) [30]. Therefore, the heat input during the friction stir welding is studied.

It is difficult to establish the model within actual conditions, so the model studies the main factors of the heat production process and makes an ideal treatment for the less influential factors. Therefore, this model is an ideal model based on these assumptions. The following assumptions are made: (1) Ignoring latent heat of the phase change during the tissue structure transformation; (2) The thread

on the surface of the tool pin is not considered; (3) Ignoring the welding inclination to simplify the model; (4) It is assumed that the friction work is all converted into friction heat.

The tool pin and tool shoulder dimensions are shown in Figure 2. The main variables used in this article are shown in Table 1. Assuming that the tool shoulder forging force acts evenly on the shoulder area, the frictional force received on the dA area is:

$$df = \frac{\mu F}{\pi r_1^2} r dr d\theta, \tag{1}$$

where F is the axial force, r_1 is the radius of the outer circumference of the tool, and μ is the coefficient of friction. The torque and power generated on the dA area are:

$$dM = \frac{\mu F}{\pi r_1^2} r^2 dr d\theta, \tag{2}$$

$$dp = dM\omega = \frac{\mu F}{\pi r_1^2} r^2 dr d\theta \omega, \tag{3}$$

where ω is the rotational angular speed. For the integration of both sides of Equation (3), the total heat production power of the shoulder zone is:

$$P_1 = \int_{r_2}^{r_1} \int_0^{2\pi} dp, \tag{4}$$

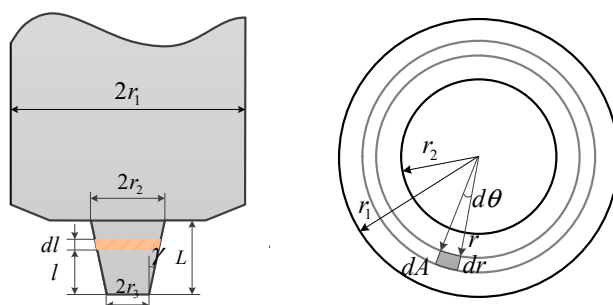


Figure 2. Schematic diagram of the pin and tool shoulder size.

Table 1. Variables used in this article.

Variables	Physical Meanings	Variables	Physical Meanings
F (N)	Axial force	σ_s (MPa)	Yield stress of the material
ω (rad)	Rotational angular speed	L (m)	Length of the tool pin
r_1 (m)	Radius of the outer circumference	σ'_{ij} (MPa)	Deviatoric stress component
r_2 (m)	Maximum radius of tool pin	$\bar{\epsilon}$ (s ⁻¹)	Strain rate component
r_3 (m)	Radius of the end of the tool pin	λ (J)	Large penalty factors
μ (J)	Coefficient of friction	F_i (N)	Arbitrary variables
γ (°)	Taper angle of the tool pin	$\bar{\sigma}$ (MPa)	Flow stress
τ (Pa)	Ultimate shear strength of the material	m (J)	The rate sensitivity
T (°C)	The temperature	$(\rho_i \text{ cm}^{-2})$	Dislocation density

Therefore, the surface heat flux density of the tool shoulder area is:

$$q_1 = \frac{P_1}{\pi(r_1^2 - r_2^2)}, \tag{5}$$

The friction force on the pin side dl is:

$$df_2 = 2\pi\tau(r_3 + l \tan \gamma)dh, \quad (6)$$

$$\tau = \frac{\sigma_s}{\sqrt{3}}, \quad (7)$$

where r_3 is the radius of the end of the tool pin, γ is the taper angle of the tool pin, τ is the ultimate shear strength of the material, and σ_s is the yield stress of the material. The torque and power of dl are:

$$dM_2 = \frac{2\pi\sigma_s(r_3 + l \tan \gamma)^2 dl}{\sqrt{3}}, \quad (8)$$

$$dp_2 = \frac{2\pi\sigma_s\omega(r_3 + l \tan \gamma)^2 dl}{\sqrt{3}}, \quad (9)$$

By integrating Equation (9), the heat production power on the side of the pin is obtained.

$$P_2 = \int_0^L dp = \frac{4\pi^2 n \sigma_s L}{3\sqrt{3}} (3r_3^2 + 3r_3 L \tan \gamma + L^2 \tan^2 \gamma), \quad (10)$$

where L is the length of the tool pin. The heat generation at the bottom surface of the pin is similar to that at the tool shoulder. The heat generation is as follows:

$$P_3 = \int_0^{r_3} \frac{\mu F}{\pi r_1^2} 2\pi r dr \times \omega r = \frac{4\mu F \pi n r_3^3}{3r_1^2}, \quad (11)$$

The body heat flux density of the tool pin is:

$$q_2 = \frac{P_2 + P_3}{V}, \quad (12)$$

$$V = \frac{\pi L(r_2^2 + r_2 r_3 + r_3^2)}{3}, \quad (13)$$

2.2. Finite Element Model

2.2.1. Geometric Model and Boundary Conditions

The FSW process is a dynamic nonlinear analysis based on the Lagrange method. The finite element software DEFORM-3D (V10.2, Scientific Forming Technologies Corporation, Columbus, OH, USA) was used to simulate the whole process of friction stir welding. The material of the tool was W6, and the workpiece size was 150 mm × 100 mm × 6 mm for a 2A14-T6 lightweight aluminum alloy. The tool shoulder diameter of the tool is 16.3 mm, the maximum diameter of the tool pin is 8.15 mm, and the length of the tool pin is 5.65 mm.

The geometric model of the friction stir welding is shown in Figure 3. To make the simulation results more accurate, three sets of meshes are added to the workpiece weld area, and the minimum mesh is divided into 0.6 mm. Because the pin participates in the material flow of the welding process, the tool plays an important role in the flow of the material. However, considering the solution duration, the mesh size of the tool shoulder and the welding influence area are gradually increased, which ensures the calculation accuracy and improves the calculation efficiency [31]. A set of mesh window is also set on the tool, and the mesh window is set to move synchronously with the tool during the welding process.

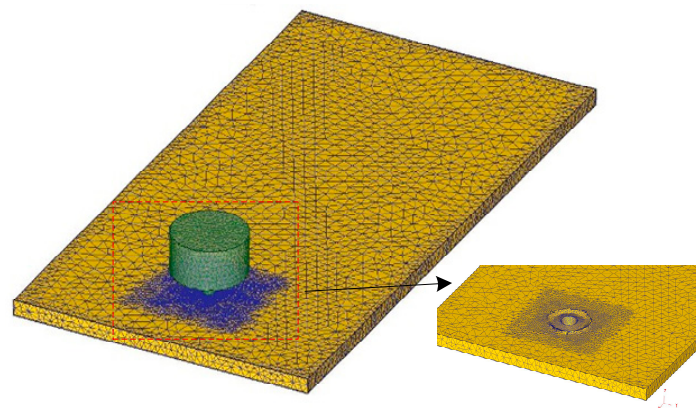


Figure 3. Geometric model in finite element model (FEM) simulation.

Due to the large plastic deformation of the material that is to be welded during the FSW process, the mesh adaptive re-division technique can be used to control the mesh distortion caused by the rotation and translation of the tool. The mesh distortion is controlled by the absolute minimum mesh size. The absolute mesh size can ensure the accuracy of the solution but also increase the solution time [32]. The total number of workpiece tetrahedral elements is divided into 68,762. The total number of mixing head tetrahedral meshes is 35,104. In the simulation process, since the tool material strength is much higher than the workpiece material, the tool is set as a rigid body, and the workpiece is set as a rigid plastic body. In order to simplify the model, the fixture and the backing plate are not built in the model, and the bottom and side degrees of freedom of the workpiece are fully constrained.

2.2.2. Finite Element Formula

A rigid viscoplastic model with a von-Mises yield criterion is used [33]. The finite element formula for rigid viscoplastic materials is based on the variational principle, where the allowable velocity should satisfy the conditions of compatibility and incompressibility, as shown in Equation (14):

$$\eta = \int_V E(\dot{\epsilon}_{ij})dV - \int_{S_F} F_i u_i dS, \quad (14)$$

where F_i , V , S_F and $E(\dot{\epsilon}_{ij})$ are respectively the surface traction force, the workpiece volume, the force surface and the plastic deformation power function. A penalty function for incompressibility is added to eliminate the incompressibility constraint on the allowable velocity field. The actual velocity field can now be determined by the steady value of the variation equation [34], which is expressed as:

$$\delta\eta = \int_V \bar{\sigma} \delta \dot{\bar{\epsilon}} dV + \lambda \int_V \dot{\epsilon}_V \delta \dot{\epsilon}_V dV - \int_{S_F} F_i \delta u_i dS, \quad (15)$$

where $\dot{\bar{\epsilon}}$, $\dot{\epsilon}_{ij}$, and σ'_{ij} are the effective strain rate, strain rate component and deviatoric stress component. λ , and δu_i are, respectively, the large penalty factors and arbitrary variables. $\delta \dot{\bar{\epsilon}}_V$ and $\delta \dot{\bar{\epsilon}}$ represent the change in the strain rate derived from δu_i .

2.2.3. Material Model

A proper selection of material models is critical to an accurate solution in the simulation process. The material changes from a solid state to a viscous state, so it is necessary to define a wide range of

strain, strain rate and flow stress values at temperatures. The flow stress is defined as a function of the strain, strain rate, and temperature, and Equation (16) is used to define the flow stress:

$$\bar{\sigma} = \bar{\sigma}(\varepsilon, \dot{\varepsilon}, T), \quad (16)$$

Among them, $\bar{\sigma}$ is the flow stress, ε is the strain, and T is the temperature.

The flow stress is temperature-dependent and strain rate sensitive. Figure 4 shows the flow stress curve of the 2A14 aluminum alloy [35]. The flow stress data is imported into the numerical model. As can be seen from Figure 4, the material is sensitive to the temperature at high strain rates. As the temperature rises, the flow stress decreases. The main reason for this is that the thermal vibration energy of the crystal lattice becomes larger at a high temperature and the external force required for the dislocation movement decreases. The thermal properties of the 2A14-T6 workpiece and W6 tool steel are summarized in Table 2.

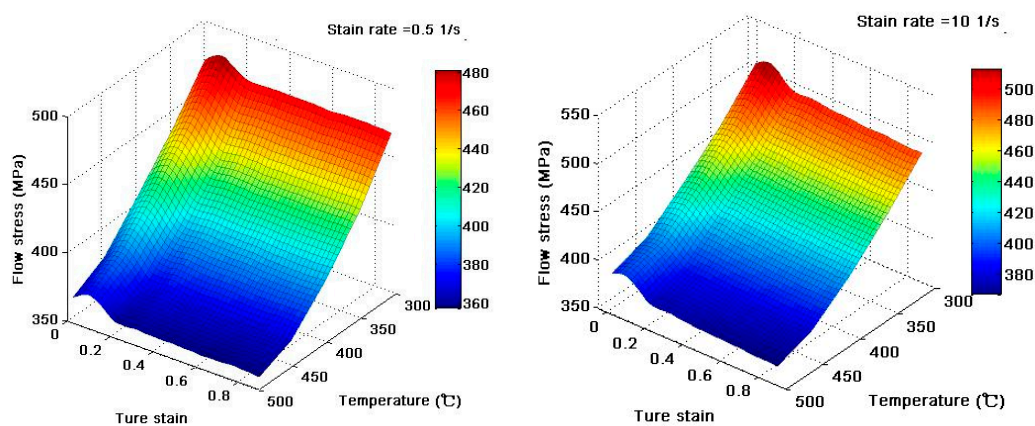


Figure 4. Flow stress curve of the 2A14 aluminum alloy.

Table 2. Thermal characteristics of the 2A14-T6 workpiece and W6 tool.

Properties	AA 2014-T6	Tool Steel W6
Heat capacity ($N/mm^2/^\circ C$)	2.46	3.18
Young's modulus (N/mm^2)	69,300	230,000
Heat expansion coefficient ($\mu mm/mm/^\circ C$)	21	11.9
Thermal conductivity ($N/s/^\circ C$)	176	30.8
Poisson's ratio (ν)	0.33	0.3

2.2.4. Dislocation Motion Model

The plastic deformation of the metal results from the dislocation movement of the material, so the dislocation density changes constantly in the process of friction stir welding, and the material flow changes based on this model. The dislocation motion is expressed as follows:

$$d\rho_i = (h - \dot{r}\rho_i)d\varepsilon, \quad (17)$$

$$h = h_0 \left(\frac{\dot{\varepsilon}}{\dot{\varepsilon}_0} \right)^m \cdot \exp\left(\frac{mQ}{RT}\right), \quad (18)$$

$$\dot{r} = \dot{r}_0 \left(\frac{\dot{\varepsilon}}{\dot{\varepsilon}_0} \right)^{-m} \cdot \exp\left(\frac{-mQ}{RT}\right), \quad (19)$$

where ρ_i is the dislocation density, h is the height of the action range of the dislocation stress field, r is the radius of the action range of the dislocation stress field, m is the rate sensitivity, and $\dot{\epsilon}_0$ is the non-dynamic strain rate.

2.3. Test Acquisition Method

The welding material used in the test is an 2A14-T6 aluminum alloy plate with the same size and simulation. The 2A14 aluminum alloy is a high-strength aerospace aluminum alloy. The internal material composition is shown in Table 3 [36]. The tool shoulder diameter is 16.3 mm, the tool cone angle is 15°, and the overall size is consistent with the simulation model parameters. The welding process is completed on a self-developed high-precision friction stir welding robot. During the welding process, the spindle speed is 900 r/min, the welding speed is 100 mm/min, and the tool shoulder is plunged against the workpiece surface by 0.2 mm. The welding inclination angle is 2.5°, after the tool needle is pressed down to a certain amount, it will dwell and rotate for 10 s. The overall welding parameters are consistent with the simulation parameters.

Table 3. Chemical composition of 2A14 Aluminum Alloys.

Cu	Si	Mn	Mg	Fe	Zn	Ti	Ni	Al
3.9~4.8	0.6~1.2	0.4~1.0	0.4~0.8	≤0.7	≤0.3	≤0.15	≤0.1	Margin

The axial force and torque in the welding process are collected by electromagnetic coupling technology, and wireless power transmission is adopted, as shown in Figure 5. Most scholars use the method of setting the mechanical sensor at the bottom of the workpiece for data acquisition. However, since the measurable area of the sensor is limited, when the welding center deviates from the center of the sensor, the accuracy of the test method will be greatly reduced; thus, it is difficult to track and collect long welds.

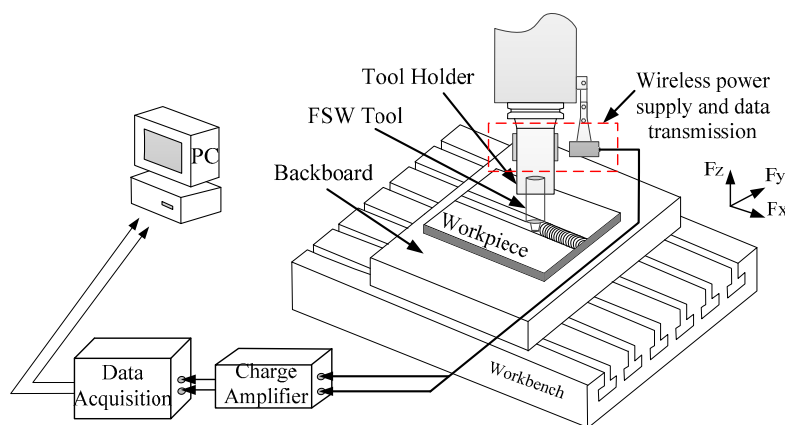


Figure 5. Signal acquisition method.

In the magnetic coupling resonant radio energy and signal transmission system, the primary side uses the amplitude shift keying (ASK) method to load the signal into the power transmission channel for a synchronous transmission, and uses the non-coherent demodulation method to extract and recover the signal on the secondary side. The schematic diagram of the acquisition method is shown in Figure 6. The power and signal synchronous transmission method can reduce the inverter link, reduce the loss and improve the quality of the advancing signal transmission.

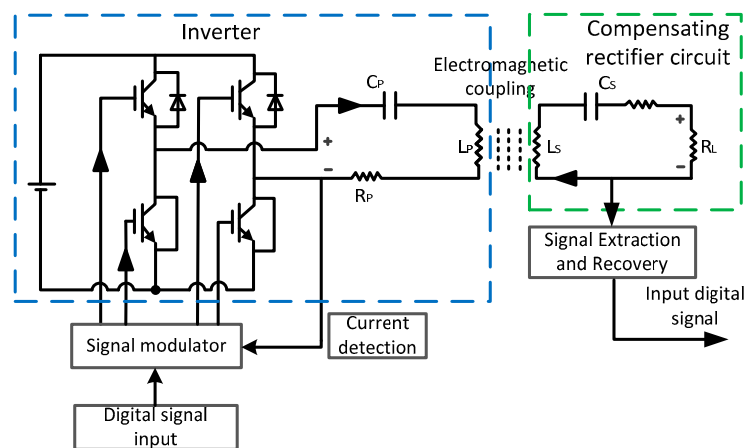


Figure 6. Schematic diagram of electromagnetic coupling signal transmission.

3. Results and Discuss

3.1. Verification of Finite Element Model

The axial force was tested throughout the FSW process. Figure 7 shows the comparison of the test results with the simulation results. It can be seen from the curve that the temperature gradually rises and reaches a peak in the first phase of the curve. In other words, the tool pin is just in contact with the workpiece, and some of the material is extruded due to plastic shear. The temperature rise softens the base material around the tool pin and promotes the pressing down of the tool. The material around the second stage tool gradually softens, and the external force of the tool plunged into the material increases slowly. In the third stage, as the tool shoulder comes into contact with the extruded material, the axial force begins to gradually increase, mainly due to the need for a greater axial force due to the tool shoulder squeezing the spilled material. At the peak of the axial force, the tool is prone to wear. Fracture can easily occur under extreme conditions. However, the axial force of the simulation output is slightly lower than the actual test results, but the overall trend of each step is in good agreement.

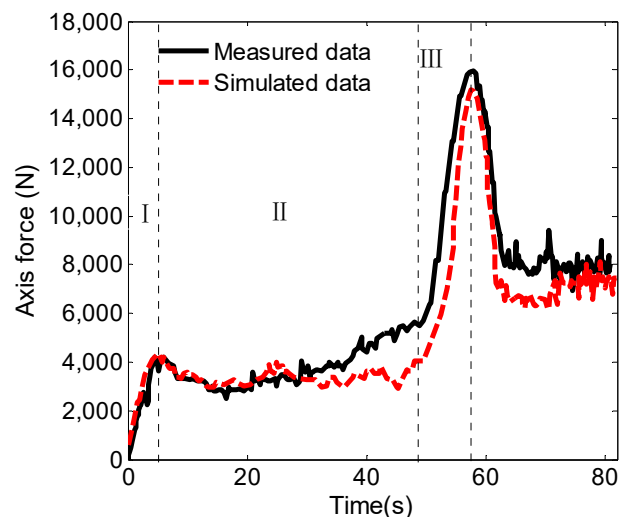


Figure 7. Axis force curve in the Z direction.

The spindle torque gives important information about the power consumption of the welding process, so torque is a decisive factor in the power requirements of the friction stir welding robot spindle. The change in the torque curve is gradual compared to the axial force, and the torque curve and the axial force curve have similar trends. As shown in Figure 8, the torque of the tool is relatively small at the beginning of the plunging. As the contact area between the tool pin and the material

increases, the spindle torque also increases. During the dwelling phase of the tool, the torque is gradually reduced, and the torque variation during the welding phase is relatively flat. The simulated data and the experimental data have certain errors, and the simulated curve changes relatively gently during the plunging phase, but the overall values and trends are close to the experimental data, thus verifying that the finite element model is relatively accurate.

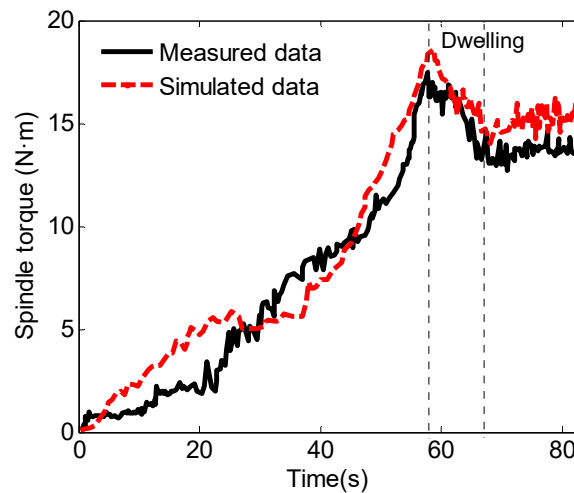


Figure 8. Spindle torque variation curve.

3.2. FSW Temperature Field Distribution

The simulation of the temperature field has a certain significance for the study of the friction stir welding process. The friction stir welding process is also the result of the joint action of the tool shoulder and the tool pin. The temperature field in the welding area is analyzed in three layers, in which the upper layer is the surface layer, the middle layer is 3.5 mm deep below the surface layer, and the bottom layer is the bottom surface of the workpiece. As shown in Figure 9, the temperature field in the surface layer presents the highest temperature, and one can observe that the temperature on the advancing side is significantly higher than that on the retreating side. The temperature on the advancing side is about 20 °C higher than that on the retreating side near the welding seam; furthermore, the experimental test can be referred to [26].

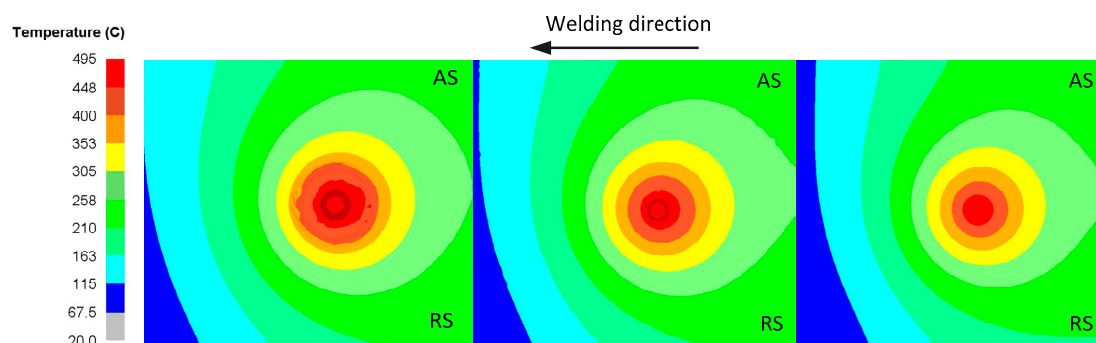


Figure 9. Temperature distribution of different thickness layers of the joint.

There is a thin layer of high temperature around the interface between the tool and the material that is to be welded. The material temperature in this area is about 500 °C. The rheological resistance of this area is extremely low, and the material is in a viscous state, which constitutes a viscous layer. The material temperature of the outer part of the viscous layer is about 450 °C, and the material is in a thermoplastic state, which constitutes a thermoplastic layer [37]. Since the tool pin is conical, the contact surface of the middle layer tool pin becomes smaller, and the temperature of the middle layer

material, in which the temperature radiation area is also relatively reduced, decreases; furthermore, the plastic softening layer area of the material decreases. Similarly, in the welding area, the contact surface of the bottom tool pin is the smallest, the welding temperature of the tool pin at the bottom is relatively low, and the material flow speed also decreases, which is one of the reasons for the welding defects at the bottom.

The temperature profile of the temperature distribution is obtained from the upper and lower temperature gradients. The temperature field simulation of the friction stir welding process can determine the temperature distribution of different thickness layers. The temperature field directly affects the material flow, and the shearing action of the tool pin drives the plastic softening layer material flow. Therefore, the effect of the temperature on the material flow in different areas of the weld can be further studied.

3.3. Material Flow

The material flow occurs in the weld area during the friction stir welding. However, the plunging process is an important process of the friction stir welding. The material softens and plastically deforms during this process. With the increasing temperature in the welding zone, the material flows plastically. Studying the material flow is helpful for understanding the welding seam forming rule and for preventing welding defects. In this study, a particle tracking technique was used to study the material flow.

The plastic flow of materials in the simulation analysis process easily causes an excessive deformation of the cell shape, which leads to distortion. Therefore, it is guaranteed that the material can continue to operate after a large plastic deformation. DEFORM-3D will automatically re-divide the distorted mesh after the mesh distortion reaches a certain level, and will generate a new high-quality mesh. The mesh re-division technique can be used to reconstruct the plastically deformed mesh in time, so that it can be used to study the plastic flow of the materials.

3.3.1. Material Flow inside the Tool Pin

Before the tool pin is not plunged, as shown in Figure 10, three sets of tracking particles are arranged inside the tool pin, where P1–P8 particles are arranged in the center area of the tool pin, P1 is set on the surface of the workpiece, and the minimum diameter of the tool pin end is 4.6 mm. P9–P16 is set in the retreating side area 2 mm away from the axis, and the rest, P17–P24, is set in the symmetrical advancing side area. Where the plunging direction is the negative direction of the Z-axis, the spindle does a rotation movement around the Z axis, and the welding direction is the negative direction of the X-axis. Therefore, the top view, front view and side view are the positive Z direction, positive X direction and negative Y direction, respectively.

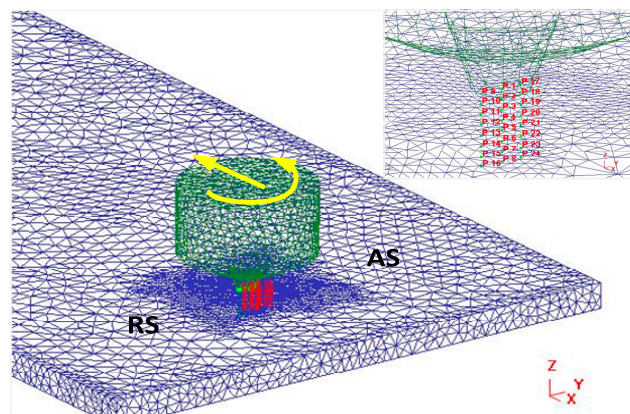


Figure 10. Setting of tracking particles inside the tool pin.

Figure 11 shows that during the pressing process, the particles (P1–P8) at the axis do not rotate around the tool pin but are squeezed to the bottom of the keyhole created by the tool pin. The reason for this phenomenon is that the linear velocity generated by the tool pin at the axial position is small, and the material fails to participate in the stirring action. After plunging onto the given amount, some of the particles inside the tool pin rotate to the top of the material, and some of the particles are distributed below the material.

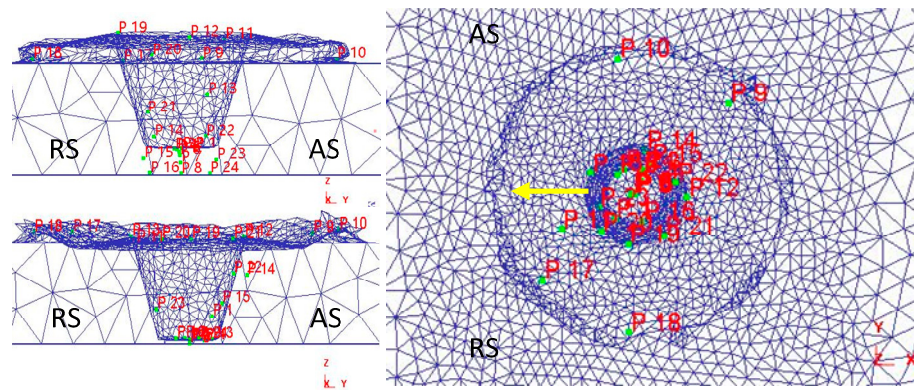


Figure 11. Tool needle internal particle plunging process.

Figure 12a,b shows that in the welding stage, the plastic material flows with the pin rotation motion. The particles undergo multiple rotational movements and are finally deposited behind the tool pin. A part of the material stays in the outer edge of the weld seam under the forging of the tool shoulder. A small number of particles follow the shoulder of the tool, and most of the material is deposited behind the weld zone, with a material distribution on both the retreating side and the advancing side. For example, both P10 and P18 particles flow around the tool shoulder. The P10 particles eventually stay on the retreating side of the weld, while the P18 particles stay on the advancing side of the weld. At the same time, due to the extrusion of the tool pin, a part of the material is deposited on the bottom of the tool pin.

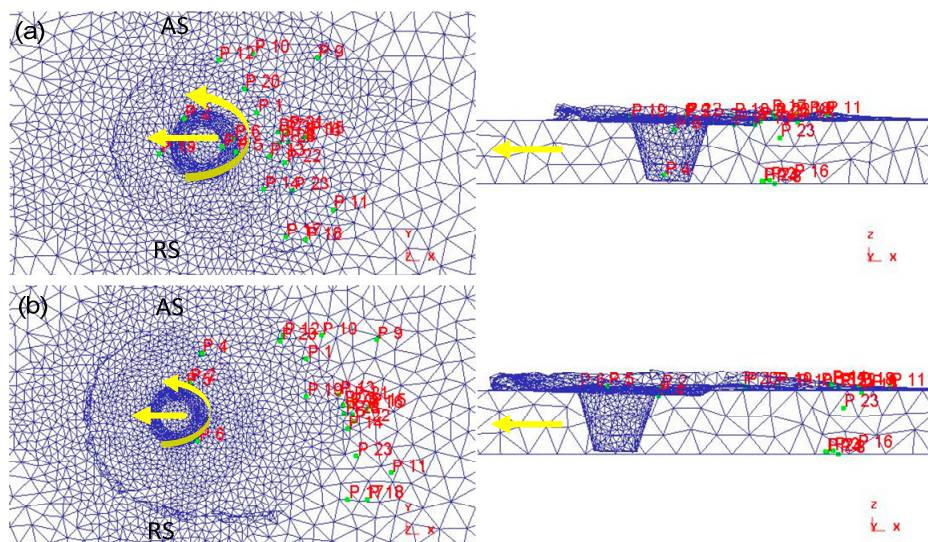


Figure 12. Material flow inside the tool needle during the welding phase. (a) Particle flow during welding; and (b) particle deposition behind the tool needle.

3.3.2. Material Flow on the Advancing Side

The tracking particles are arranged on the advancing side of the welding area. In order to improve the comprehensiveness of the simulation analysis, two sets of tracking particles (P1–P8 and P9–P16) are set. The distance from the axis of the tool pin is 3 mm, and the two groups of tracking particles are symmetrically distributed, as shown in Figure 13. It can be seen from the side view that they are located on both sides of the center line of the tool pin.

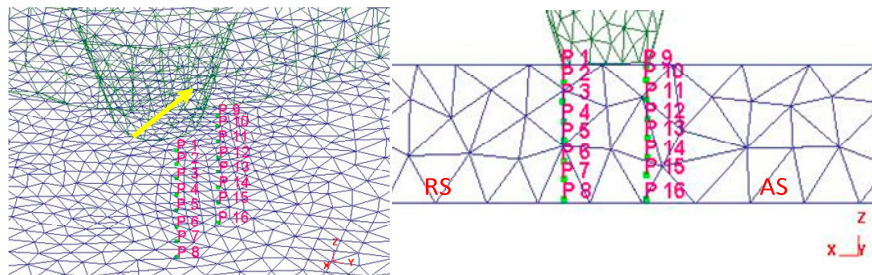


Figure 13. Advancing side tracking particle position setting.

During the plunging process, the particles on the advancing side differ from the flow of particles in the tool pin. During this stage, the particles are not rotated around the tool pin in the initial stage of pressing, but are squeezed by the tool pin to both sides of the tool pin, as shown in Figure 14. A plastic softening layer is formed, and the plastic softening zone becomes larger in the late stage of the plunging stage; the particles flow with the tool, the upper layer particles are spiraled to the upper side of the material and are finally moved to the advancing side behind the welding, and most of the other particles remain on the retreating side.

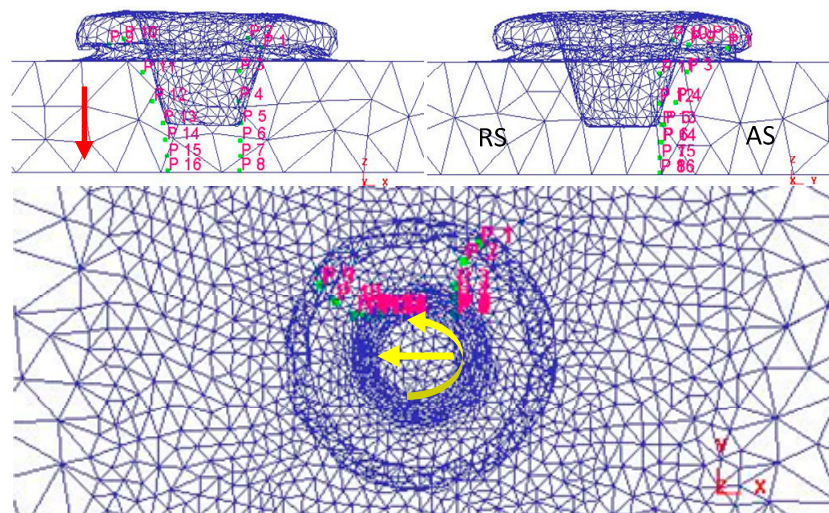


Figure 14. The trend of the particle flow during pressing.

Figure 15a,b shows that the particles P6, P7, and P8 are found behind the welding advancing side during the welding process. During the plunging process, the particles are plunged by the tool pin into the opposite direction of the welding, but the distance from the end of the tool pin becomes farther. The diameter of the end of the tool pin is small, and the effective influence area is smaller. Therefore, only a small part of the displacement of the three particles occurs during the welding process, and it cannot participate in the material flow.

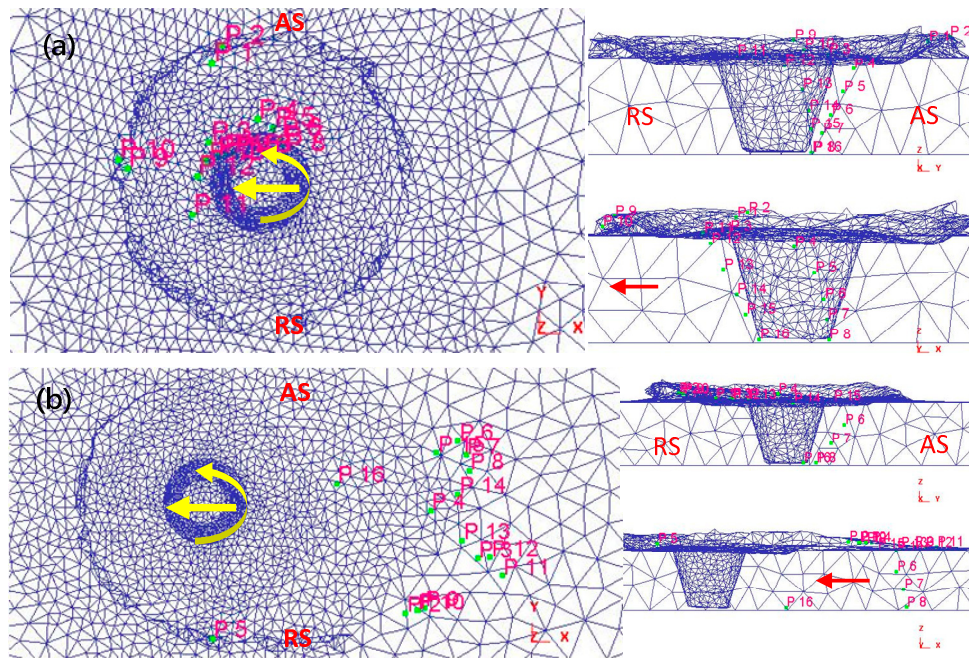


Figure 15. Material flow on the advancing side. (a) The tool is pressed down onto the given amount; and (b) the particles are deposited behind the tool.

Figure 15b shows that most of the tracking particles on the advancing side are rotated by the tool pin to the vicinity of the centerline of the weld bead behind the tool, and then gradually deposited at different positions between the center of the weld and the retreating side, which has also been observed in the experiment [38]. More particles were distributed near the retrograde side, and it was also confirmed that more materials flowed to the retreating side than to the advancing side. At the same time, partial backflow occurs due to the tool shoulder material, and finally the tool shoulder is forged to the rear of the tool.

3.3.3. Material Flow on the Retreating Side

Two sets of tracking particles are arranged on the retreating side, and the position is symmetrical to the advancing side. P1–P8 is close to the leading edge of the tool, and P9–P16 is close to the trailing edge of the tool. Since the rotation direction of the tool is counterclockwise, the particles in the initial stage of pressing extend outward under the extrusion action of the tool pin, as shown in Figure 16. As the pressing temperature gradually increases, the plastic softening layer in the weld zone becomes thicker, and the material plastically flows. The particles in the P1 group move backwards to the rear of the weld with the rotation of the tool pin.

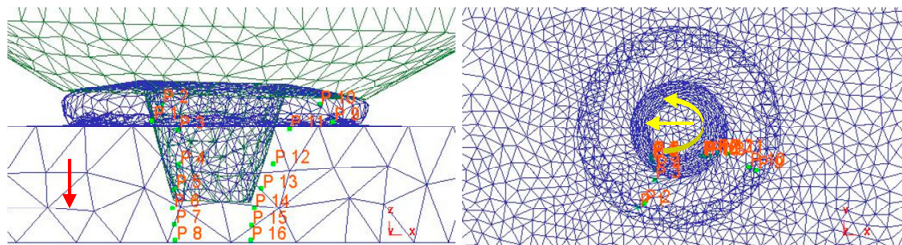


Figure 16. Particle migration during the plunging stage.

Figure 17a,b shows that the material flows under the action of the tool pin, whereas the material flow velocity on the retreating side is less than the advancing side, which also results in less material accumulating on the advancing side, which confirms the results of the literature [39]. The trajectory of

the marker material particles on the return side has two main parts. A part of the material is rotated around the tool pin for about half a week and then deposited onto the area near the advancing side of the tool. The other part of the material hardly rotates around the tool pin, but is gradually pushed down by the tool onto the area between the center line and the retreating side of the rear weld. A small number of particles on the tool shoulder is deposited in front of the retreating side after rotating around the tool for several weeks.

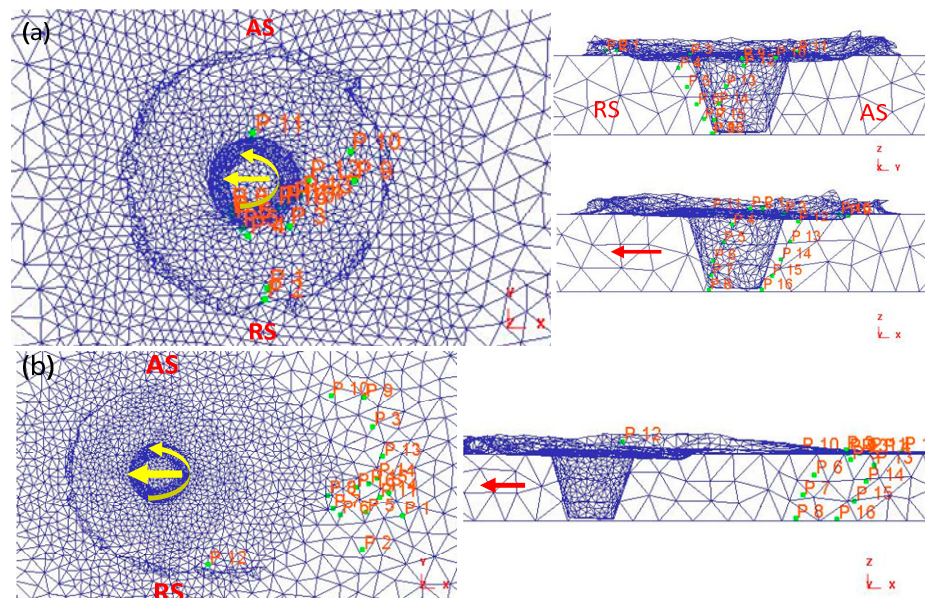


Figure 17. Material flow on the retreating side. (a) The tool is pressed down onto the given amount; and (b) the particles are deposited behind the tool.

3.4. Prediction of Welding Defects

Friction stir welding is a solid phase joining technique. Welding defects will also occur if improper welding parameters lead to an abnormal material flow. Two kinds of welding defects of the joint appeared in many simulation attempts.

The formation of hole defects is mainly due to insufficient heat input in the welding process, insufficient materials reaching the plastic softening state and an insufficient material flow, resulting in an incomplete closure in the welding interior [40]. When the spindle speed is low or the welding speed is too fast, the joint is prone to holes and crack defects. This type of weld defect is usually located in the middle and lower parts of the advancing side and near the weld surface. In the simulation process, the holes that were found after the welding speed increased by 2 times were formed in the lower parts of the advancing side, as shown in Figure 18b. When the rotation speed of the main shaft is further reduced by 0.5 times, a crack defect occurs after the welding, as shown in Figure 18a.

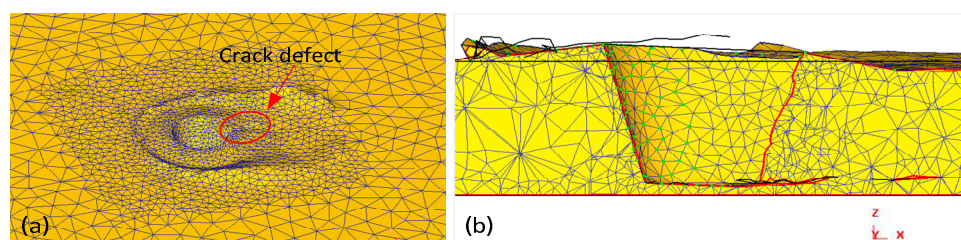


Figure 18. Simulation of the formation of weld defects. (a) Crack defects; and (b) hole defects.

According to the above research on the material flow, during the welding process the material flows from the advancing side to the retreating side of the material, and the material on the retreating

side flows less to the advancing side. However, when the material flow is abnormal, the material on the rear side of the tool is difficult to fill in time, which will lead to the generation of holes. Therefore, in order to avoid the appearance of holes and cracks in the joint during the welding, it is very important to optimize the welding process parameters. A finite element analysis can effectively predict the welding defects. In this paper, the formation of welding defects is predicted by the law of material flow. Welding defects themselves are not expected to occur. This paper mainly studies the law of material flow, so the detailed study of welding defects will be carried out in the following work.

3.5. Effect of Material Flow on Microstructure

Figure 19 shows a comparison of the simulated temperature field and the metallographic structure of the joint cross section. It can be seen from the observation that the weld nugget zone (WNZ, zone I) in the cross section of the friction stir welding joint is connected with the thermo-mechanically affected zone (TMAZ, zone II). The heat affected zone (HAZ, zone III) is adjacent to the thermo-mechanically affected zone. In the simulation model, the temperature in the contact area with the tool is relatively high and gradually decreases to both sides.

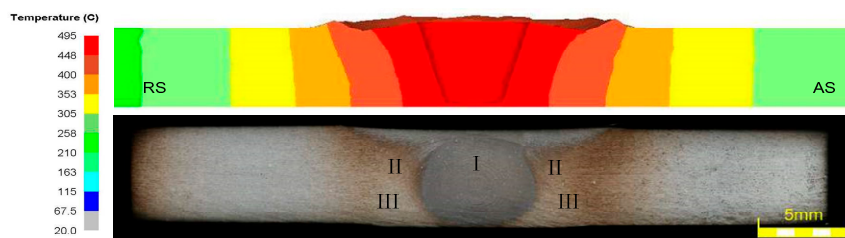


Figure 19. Cross-sectional comparison of the joints.

Due to the different material flows and microstructures in each region of the joint, the WNZ of the material forms a clear boundary with the TMAZ, and the material flow direction can be clearly seen from the formation of the microstructure in the TMAZ. As shown in Figure 20b, the microstructure in the WNZ is composed of fine recrystallized grains due to the intense stirring action of the pin. At the same time, it can be observed that the material in the TMAZ also has a plastic flow. The material under TMAZ near WAZ is rotated by the tool pin, and the material has an upward flow trend. Some of the material is squeezed into the WNZ, which is also found in the simulation. The material in TMAZ far away from the WNZ tends to move obliquely upward, and shows a similar rule on the advancing side, as shown in Figure 20a. However, it can be observed that the material flow slope on the advancing side is larger, which also confirms that the material flow on the advancing side is more intense.

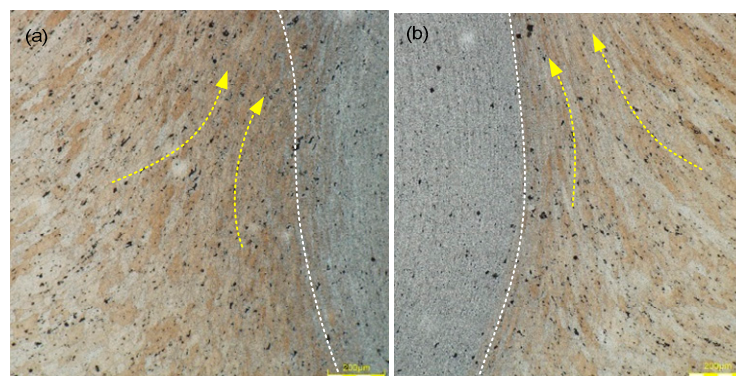


Figure 20. The boundary and material flow between the weld nugget zone (WNZ) and the thermo-mechanically affected zone (TMAZ). (a) The boundary area between the WNZ and the TMAZ on the advancing side; and (b) the boundary area between the WNZ and the TMAZ on the retreating side.

Figure 21a shows that the material flows obliquely to the weld nugget region above the TMAZ, and that the material in the tool shoulder action region has a slight flow trend. However, it can be seen from Figure 21b that a triangular region of material flow appears on the upper part of the advancing side due to the joint action of the tool pin and the tool shoulder. Here, the upper part of the weld has a downward flow trend under the extrusion of the tool shoulder. The simulation process also observed the action process of the tool shoulder. The action of the tool shoulder is more intense on the retreating side. The three-directional flows of the TMAZ material, tool shoulder action zone material and the WNZ material meet sharply. At the same time, if the material flow is abnormal in this area, weld defects will easily occur.

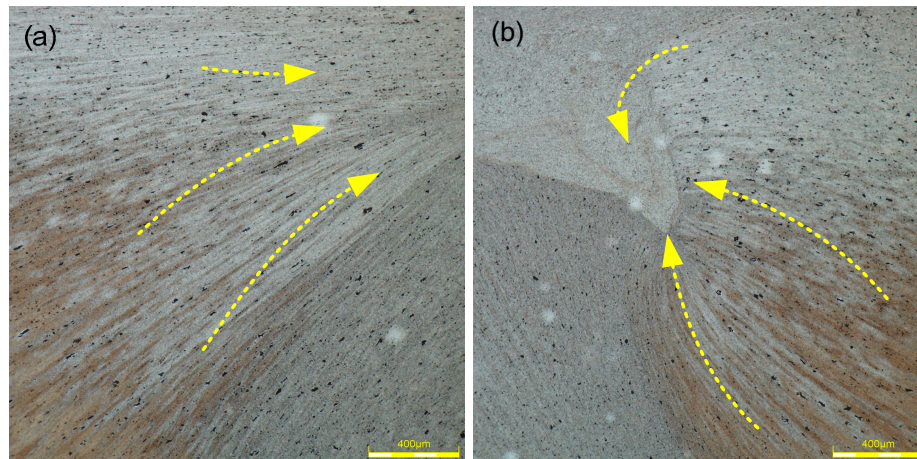


Figure 21. The material flow intersection of the welded joint. (a) The material intersection on the advancing side; and (b) the material intersection on the retreating side.

4. Conclusions

In this paper, the thermogenic physical model of the FSW process is established, and the finite element model of FSW is established. The material flow and temperature field in the welding process are studied by a numerical simulation. The finite element model is updated by the results of the axial force and torque tests. Moreover, the overall trend of the material flow in a finite element analysis is verified by the experiments on the weld cross section. The correctness of the finite element model analysis is verified by the microstructure formation and flow trend. Based on the results of this study, the following conclusions were made:

- (1) The thermogenic physical model of the FSW process is established, and the finite element model is constructed to simulate the FSW process. The axial force and torque of the friction stir welding process were collected by electromagnetic coupling technology, and the data of the test and simulation were compared. The curve trend verified the correctness of the finite element model.
- (2) Through a simulation analysis, it was found that the temperature on the advancing side is about 20 °C higher than that on the retreating side near the welding seam, and that the FSP temperature field has an important influence on the material flow field. By analyzing the temperature of the workpiece at different thickness layers, it was found that the temperature difference between the two sides of the middle and lower layers was relatively reduced.
- (3) The material flow law in different areas of the weld was studied, and it was found that a small part of the inner material of the tool pin was extruded to the bottom of the workpiece. There is a large difference in the flow conditions of the upper and lower parts of the weld. The material on the upper surface tends to move downward under the influence of the shoulder extrusion, while the material on the lower part moves spirally upward under the influence of the tool pin. The material flow amount of the advancing side is higher than that of the retreating side.

- (4) The material on the advancing side finally stays behind the weld, and most of the particles are distributed on the retreating side. The degree of the material flow gradually decreases along the thickness direction. Most of the material on the retreating side is finally distributed behind the welding seam, and some of it flows to the advancing side.
- (5) Through a simulation analysis, it was found that the abnormal material flow in the welding process is prone to welding defects under the conditions of a low rotating speed and high welding speed.
- (6) Through the comparative analysis of the cross-section of the joint, it was also found that there is a significant difference in the flow of the material between the advancing side and the retreating material, and that the material flow in the different regions makes the tissue forming boundary distinct. The tensile state of the joint microstructure can observe the flow tendency of the material. The advancing side forms a multi-directional material flow intersection area under the tool shoulder, which easily forms welding defects when the material flow is abnormal.

Author Contributions: H.L. and T.W. developed the FEM of friction stir welding process and wrote the paper; H.L., T.W. and P.W. conceived and designed the experiments; T.W. and Y.L. analyzed the data and modified the paper. T.W., F.Z. and H.W. performed the experiments.

Funding: The authors would like to acknowledge the financial support from the National Natural Science Foundation of China (Grant No. 51505470), the Youth Innovation Promotion Association, CAS and 'JXS' innovation fund, SIA.

Conflicts of Interest: The authors declare no conflict of interest.

References

1. Wang, T.; Zou, Y.; Matsuda, K. Micro-structure and micro-textural studies of friction stir welded AA6061-T6 subjected to different rotation speeds. *Mater. Des.* **2016**, *90*, 13–21. [[CrossRef](#)]
2. Morita, T.; Yamanaka, M. Microstructural evolution and mechanical properties of friction-stir-welded Al-Mg-Si joint. *Mater. Sci. Eng. A* **2014**, *595*, 196–204. [[CrossRef](#)]
3. Guo, J.F.; Chen, H.C.; Sun, C.N.; Bi, G.; Sun, Z.; Wei, J. Friction stir welding of dissimilar materials between AA6061 and AA7075 Al alloys effects of process parameters. *Mater. Des.* **2014**, *56*, 185–192.
4. Zhang, H.; Wang, M.; Zhang, X.; Yang, G. Microstructural characteristics and mechanical properties of bobbin tool friction stir welded 2A14-T6 aluminum alloy. *Mater. Des.* **2015**, *65*, 559–566. [[CrossRef](#)]
5. Carlone, P.; Palazzo, G.S. Influence of process parameters on microstructure and mechanical properties in AA2024-T3 friction stir welding. *Metall. Microstruct. Anal.* **2013**, *2*, 213–222. [[CrossRef](#)]
6. Su, H.; Wu, C.S.; Bachmann, M.; Rethmeier, M. Numerical modeling for the effect of pin profiles on thermal and material flow characteristics in friction stir welding. *Mater. Des.* **2015**, *77*, 114–125. [[CrossRef](#)]
7. Tutunchilar, S.; Haghpanahi, M.; Besharati Givi, M.K.; Asadi, P.; Bahemmat, P. Simulation of material flow in friction stir processing of a cast Al-Si alloy. *Mater. Des.* **2012**, *40*, 415–426. [[CrossRef](#)]
8. Chen, Z.W.; Pasang, T.; Qi, Y. Shear flow and formation of nugget zone during friction stir welding of aluminium alloy 5083-O. *Mater. Sci. Eng. A* **2008**, *474*, 312–316. [[CrossRef](#)]
9. Zhu, Y.; Chen, G.; Chen, Q.; Zhang, G.; Shi, Q. Simulation of material plastic flow driven by non-uniform friction force during friction stir welding and related defect prediction. *Mater. Des.* **2016**, *108*, 400–410.
10. Assidi, M.; Fourment, L.; Guerdoux, S.; Nelson, T. Friction model for friction stir welding process simulation: Calibrations from welding experiments. *Int. J. Mach. Tools. Manuf.* **2010**, *50*, 143–155. [[CrossRef](#)]
11. Zhang, Z.; Wu, Q. Numerical studies of tool diameter on strain rates, temperature rises and grain sizes in friction stir welding. *J. Mech. Sci. Technol.* **2015**, *29*, 4121–4128. [[CrossRef](#)]
12. Chowdhury, S.M.; Chen, D.L.; Bhole, S.D.; Cao, X. Tensile properties of a friction stir welded magnesium alloy: Effect of pin tool thread orientation and weld pitch. *Mater. Sci. Eng. A* **2010**, *527*, 6064–6075. [[CrossRef](#)]
13. Yang, C.L.; Wu, C.S.; Lv, X.Q. Numerical analysis of mass transfer and material mixing in friction stir welding of aluminum/magnesium alloys. *J. Manuf. Process.* **2018**, *32*, 380–394. [[CrossRef](#)]
14. Tongne, A.; Desrayaud, C.; Jahazi, M.; Feulvarch, E. On material flow in Friction Stir Welded Al alloys. *J. Mater. Process. Tech.* **2017**, *239*, 284–296. [[CrossRef](#)]

15. Mironov, S.; Masaki, K.; Sato, Y.S.; Kokawa, H. Relation between material flow and abnormal grain growth in friction-stir welds. *Scripta Mater.* **2012**, *67*, 983–986. [[CrossRef](#)]
16. Franke, D.J.; Zinn, M.R.; Pfefferkorn, F.E. Intermittent Flow of Material and Force-Based Defect Detection During Friction Stir Welding of Aluminum Alloys. *Fri. Stir Weld. Process. X* **2019**, 149–160.
17. Gratecap, F.; Girard, M.; Marya, S.; Racineux, G. Exploring material flow in friction stir welding: Tool eccentricity and formation of banded structures. *Int. J. Mater. Form.* **2012**, *5*, 99–107. [[CrossRef](#)]
18. Huang, Y.; Wang, Y.; Wan, L.; Liu, H.; Shen, J.; dos Santos, J.F.; Zhou, L.; Feng, J. Material-flow behavior during friction-stir welding of 6082-T6 aluminum alloy. *Int. J. Adv. Manuf. Tech.* **2016**, *87*, 1115–1123. [[CrossRef](#)]
19. Dialami, N.; Chiumenti, M.; Cervera, M.; Agelet de Saracibar, C.; Ponthot, J.P.; Bussetta, P. Numerical Simulation and Visualization of Material Flow in Friction Stir Welding via Particle Tracing. *Numer. Simul. Coupl. Probl. Eng.* **2014**, *33*, 157–169.
20. Li, W.-Y.; Li, J.-F.; Zhang, Z.-H.; Gao, D.-L.; Chao, Y.-J. Metal flow during friction stir welding of 7075-T651 Aluminum alloy. *Exp. Mech.* **2013**, *53*, 1573–1582. [[CrossRef](#)]
21. Shanavas, S.; Dhas, J.E.R. Quality Prediction of Friction Stir Weld Joints on AA 5052 H32 Aluminium Alloy Using Fuzzy Logic Technique. *Mater. Today Proc.* **2018**, *5*, 12124–12132. [[CrossRef](#)]
22. De Filippis, L.A.C.; Serio, L.M.; Facchini, F.; Mummolo, G.; Ludovico, A.D. Prediction of the Vickers Microhardness and Ultimate Tensile Strength of AA5754 H111 Friction Stir Welding Butt Joints Using Artificial Neural Network. *Materials* **2016**, *9*, 915. [[CrossRef](#)] [[PubMed](#)]
23. Cisco, A.B.; Jordon, J.B.; Avery, D.Z.; Liu, T.; Brewer, L.N.; Allison, P.G.; Carino, R.L.; Hammi, Y.; Rushing, T.W.; Garcia, L. Experiments and Modeling of Fatigue Behavior of Friction Stir Welded Aluminum Lithium Alloy. *Metals* **2019**, *9*, 293. [[CrossRef](#)]
24. Zhang, Z.; Xiao, B.L.; Wang, D.; Ma, Z.Y. Effect of Alclad Layer on Material Flow and Defect Formation in Friction-Stir-Welded 2024 Aluminum Alloy. *Metall. Mater. Trans. A* **2011**, *42*, 1717–1726. [[CrossRef](#)]
25. Zhu, Z.; Wang, M.; Zhang, H.; Zhang, X.; Yu, T.; Wu, Z. A finite element model to simulate defect formation during friction stir welding. *Metals* **2017**, *7*, 256. [[CrossRef](#)]
26. Edwards, P.D.; Ramulu, M. Material flow during friction stir welding of Ti-6Al-4V. *J. Mater. Process. Technol.* **2015**, *218*, 107–115. [[CrossRef](#)]
27. Mao, Y.; Ke, L.; Liu, F.; Chen, Y.; Xing, L. Effect of tool pin-tip profiles on material flow and mechanical properties of friction stir welding thick AA7075-T6 alloy joints. *Int. J. Adv. Manuf. Technol.* **2017**, *88*, 949–960. [[CrossRef](#)]
28. Ji, S.D.; Shi, Q.Y.; Zhang, L.G.; Zou, A.L.; Gao, S.S.; Zan, L.V. Numerical simulation of material flow behaviour of friction stir welding influenced by rotational tool geometry. *Comp. Mater. Sci.* **2012**, *63*, 218–226. [[CrossRef](#)]
29. Luo, H.; Wu, T.; Fu, J.; Wang, W.; Chen, N.; Wang, H. Welding Characteristics Analysis and Application on Spacecraft of Friction Stir Welded 2A14-T6 Aluminum Alloy. *Materials* **2019**, *12*, 480. [[CrossRef](#)] [[PubMed](#)]
30. Sun, Z.; Wu, C.S. A numerical model of pin thread effect on material flow and heat generation in shear layer during friction stir welding. *J. Manuf. Process.* **2018**, *36*, 10–21. [[CrossRef](#)]
31. Buffa, G.; Hua, J.; Shivpuri, R.; Fratini, L. A continuum based FEM model for friction stir welding-model development. *Mater. Sci. Eng. A* **2006**, *419*, 389–396. [[CrossRef](#)]
32. Jain, R.; Pal, S.K.; Singh, S.B. A study on the variation of forces and temperature in a friction stir welding process: A finite element approach. *J. Manuf. Process.* **2016**, *23*, 278–286. [[CrossRef](#)]
33. Leal, R.M.; Leitao, C.; Loureiro, A.; Rodrigues, D.M.; Vilaca, P. Material flow in heterogeneous friction stir welding of thin aluminium sheets: Effect of shoulder geometry. *Mater. Sci. Eng. A* **2008**, *498*, 384–391. [[CrossRef](#)]
34. Jain, R.; Pal, S.K.; Singh, S.B. Finite element simulation of pin shape influence on material flow, forces in friction stir welding. *Int. J. Adv. Manuf. Technol.* **2018**, *94*, 1781–1797. [[CrossRef](#)]
35. Zhou, Z.X.; Li, Y.L.; Suo, T. Microstructure and Dynamic Mechanical Properties of 2A14 Aluminium Alloy Sheet. *Mech. Sci. Technol. Aerosp. Eng.* **2009**, *28*, 1464–1467.
36. GB/T 3880-1997. *Aluminium and Aluminium Alloy Rolled Sheet*; Standardization Administration of the People's Republic of China: Beijing, China, 1998.
37. AlRoubaiy, A.O.; Nabat, S.M.; Batako, A.D.L. Experimental and theoretical analysis of friction stir welding of Al-Cu joints. *Int. J. Adv. Manuf. Technol.* **2014**, *71*, 1631–1642. [[CrossRef](#)]
38. Masaki, K.; Saito, H.; Nezaki, K.; Kitamoto, S.; Sato, Y.S.; Kokawa, H. Material Flow and Microstructure Evolution in Corner Friction Stir Welding of 5083 Al Alloy Using AdStir Technique. *Fri. Stir Weld. Process. X* **2019**, 181–188. [[CrossRef](#)]

39. Zhang, H.J.; Liu, H.J. Characteristics and Formation Mechanisms of Welding Defects in Underwater Friction Stir Welded Aluminum Alloy. *Metallogr. Microstruct. Anal.* **2012**, *1*, 269–281. [[CrossRef](#)]
40. Kumar, K.; Kailas, S.V. The role of friction stir welding tool on material flow and weld formation. *Mater. Sci. Eng. A* **2008**, *485*, 367–374. [[CrossRef](#)]



© 2019 by the authors. Licensee MDPI, Basel, Switzerland. This article is an open access article distributed under the terms and conditions of the Creative Commons Attribution (CC BY) license (<http://creativecommons.org/licenses/by/4.0/>).